

Compliant and Hard Cu(Ni)-C Nanocomposite Coatings

Eric Brannigan¹ & Alan F. Jankowski¹

¹Edward E. Whitacre, Jr. College of Engineering, Dept. of Mechanical Engineering, Texas Tech University, USA
Correspondence: Alan F. Jankowski, Texas Tech University, Mechanical Engineering, Box 41021, 7th and Boston, Lubbock, TX 79409, USA. Tel: 1-806-742-3563. E-mail: alan.jankowski@ttu.edu

Received: January 8, 2013 Accepted: January 31, 2013 Online Published: February 19, 2013

doi:10.5539/jmsr.v2n2p60

URL: <http://dx.doi.org/10.5539/jmsr.v2n2p60>

Abstract

Copper-Nickel-Carbon nanocomposite coatings are synthesized by the sequential sputter deposition of carbon (C) and a copper-nickel (Cu_{1-x}Ni_x) alloy. A distinct transition occurs as the Ni content (x) is increased from 0 to 1.00 during the Cu_{1-x}Ni_x alloy deposition. The coating morphology changes from a dispersion of metallic Cu-particles in a C matrix to a well-defined nanolaminate structure. Between these morphological forms, a new prototype nanocomposite is produced at a Ni concentration (x) of 0.1-0.4 with the appearance of an interpenetrating matrix structure of C and Cu(Ni). This morphological structure has both a high 24-27 GPa hardness (H) and a low elastic modulus (E) of 144-169 GPa that results in a record high values of H/E at 1/6 and a H^3/E^2 at 0.67-0.69 GPa in a novel compliant and hard coating.

Keywords: nanocomposite, sputter deposition, Cu(Ni)-C, hard coatings

1. Introduction

The search for protective coatings that can provide both hardness and compliance continues today as an active pursuit. In general, coatings with a high hardness (H) are accompanied by a high elastic modulus (E). Many wear resistant coatings formed with borides, carbides, and nitrides (Musil, 2000; Leyland & Matthews, 2000; Andrievskiy, 2007) have H/E ratios of 1/10 or less. Limitations are still encountered in the preparation of intrinsically very hard nanocomposite materials such as Ti-Si-N (Veprék & Veprék-Heijman, 2012) and complex alloy systems such as Al-Cr-Ta-Ti-Zr-N (Chang et al., 2010) where challenges can be found to accurately measure coating hardness (Fischer-Cripps et al., 2012) and modulus when hardness values exceed 30 GPa. The further evaluation of fracture toughness in hard coatings too requires careful assessment (Zhang & Zhang, 2012) of cracking and delamination effects. For hard coating applications, an additional attribute of greater flexibility, i.e. increased compliance, can be very useful for minimizing problems associated with coating adhesion and fracture. A common approach taken to improve the service life of hard coatings is through use of a nanocomposite structure. Common structural types are seen in particulate-reinforced matrix nanocomposites, and nanolaminates in the form of strained layered superlattices. Nanocomposite structures, i.e. nanostructured composites, in the form of a nanolaminate can be synthesized through an artificial fluctuation of composition through the vapor or aqueous deposition of layers with nanoscale thickness in one growth direction. An example (Jankowski, 2008) of the bottom-up, i.e. atomic scale, process is the physical vapor deposition method of magnetron sputtering. Nanolaminate coatings composed of boron and hexagonal boron-nitride layers were sputter deposited (Jankowski et al., 1997, 1999) to evaluate use as low-friction, high-hardness surface coatings. The inherent metastable nature to the formation process of the artificial laminate nanostructure gives rise to physical properties, such as magnetic and optical, that can be engineered far from equilibrium. Common to each nanolaminate is the interface structure and the periodic distribution of interfaces along the direction of deposition-induced composition fluctuation. The ability to form a well-defined layered structure is affected by the chemical solubility of constituent elements as well as superlattice distortions. Both of these attributes are found in the copper-nickel-carbon material system as was reported previously (Jankowski & Stearns, 1991) for use as an optical coating to reflect x-rays. Copper (Cu) and carbon (C) are immiscible. However, nickel (Ni) and carbon have a limited solid solubility with one another and can form a metastable ordered phase. It was observed that the morphology of the Cu(Ni) nanostructure changes as alternatively deposited with C from a ceramic-metal, i.e. cermet, nanocomposite where nanoparticles are dispersed within a matrix, to a distinct nanolaminate structure as the Ni concentration is increased within the Cu layer.

A material system with morphological changes by design, through control of composition, provides an opportunity to now examine the simultaneous effects that morphology has on both the elastic and plastic behavior. That is, to explore whether or not a transition state in morphology can be advantageous for enhancing compliance without sacrificing hardness. The effects that chemical solubility has on the morphology at the nanoscale, and the corresponding mechanical properties of nanocrystalline Cu(Ni)-C are now assessed using x-ray diffraction, electron microscopy, nanoindentation, and tapping-mode force microscopy. High-resolution lattice images taken of specimens prepared in a cross-section view reveal the nanoscale growth morphology. The hardness (H) and elastic modulus (E) of each structure is measured by conventional nanoindentation, and for independent confirmation through tapping-mode force microscopy, i.e. where the frequency shift of an oscillating cantilever tip in contact with the nanocomposite is related to the reduced modulus (E^*).

2. Experimental Methods

2.1 Synthesis and Structural Characterization

The deposition of different 0.15-0.3 μm thick nanocomposite coatings onto Si(111) substrate wafers is accomplished (Jankowski & Stearns, 1991) by the sequential sputtering of carbon C targets and a composite target of copper (Cu) and nickel (Ni) using planar magnetrons as operated in the dc mode. The exposure of the Si substrate is cycled alternately between the 0.05-0.2 $\text{nm}\cdot\text{s}^{-1}$ fluxes from the C sources and composite Cu(Ni) source, respectively. In this way, a number (N) of nominal layer pairs that comprise the nominal nanolaminate with a characteristic layer-pair repeat spacing, i.e. composition wavelength (λ), equals the summation of the component layer thicknesses (ℓ) of the C and Cu(Ni) layers. Several different $\text{Cu}_{1-x}\text{Ni}_x$ layers are considered in synthesizing the Cu(Ni)-C nanocomposite coatings as, e.g., at x equals 0.00, 0.12, 0.34, 0.45, and 1.00. The deposition of the coating is completed with a thin 2 nm thick cap (top) layer of C that functions to prevent oxidation of the metals within the nanocomposite. A working gas of pure argon (Ar) is used at a 0.67 Pa sputtering pressure and a 26 $\text{cm}^3\cdot\text{s}^{-1}$ flow rate. The C target is operated at 450-500 W power and a 415-525 V discharge whereas the Cu, Cu(Ni) and Ni targets are operated at 35-50 W power and 250-300 V discharge. A 10 cm working distance between the magnetron sources and the water-cooled substrate table provides the condition for thermalization of the sputtered neutrals that minimizes (or eliminates) intermixing between component layers at their interfaces as would be attributed solely to energetic bombardment effects. Also, the effects of chemical gradients, phase separation, and strain energy contributions can influence the structural morphology during growth of the nanocomposite structure.

The structure of the cermet nanocomposite coatings is characterized using two basic methods. High resolution, transmission electron microscopy (HREM) of the coatings prepared for cross-section view (Jankowski & Stearns, 1991) is used to assess the layer morphology and scale of nanostructured features. X-ray diffraction (XRD) analysis is pursued to further quantify features as layer dimensions, interface roughness, and crystalline structure. Here, a Rigaku Miniflex II diffractometer is operated both at glancing angle of incidence and high angle in the $\theta/2\theta$ mode using monochromatic radiation. The 8.04 keV, Cu k_α radiation is produced from a 25 keV, 15 mA electron beam directed onto a water cooled Cu anode. The Bragg reflections at high angle provide evidence of crystalline structure and growth orientation. The reflectivity patterns at glancing angles of incidence provide details of short range order. For comparison with experimental results, the glancing angle scans can be simulated at the open-access user website (http://henke.lbl.gov/optical_constants/multi2). The program code uses the Fresnel equations and Kohn's (1995) analytic formulae to model the layer-pair repeat spacing (λ), the component-layer pair thickness ratio (I), and the root-mean square (*rms*) interface roughness (σ). In this analysis, the position of the 2θ peak is determined primarily by λ , the ratio of the intensity between higher order reflections is most affected by σ , and the absolute reflected intensity of the reflection as affected by I .

2.2 Mechanical Property Measurements

The mechanical measurements are made using dynamic nanoindentation test methods that are based upon Hertzian contact mechanics. In one test method, the conventional nanoindentation test and Oliver-Pharr analysis (1992, 2004) is used to determine the hardness (H) subsequent to plastic deformation of the test surface by indentation from a Berkovich diamond tip. The Young's modulus (E) is computed from the reduced elastic modulus (E^*) as computed by a proportional linear fit of the unloading stiffness (S) in the initial portion of the power-law unloading curve. The contact depth (h_c) is the projected depth by linear unloading from the maximum load (P_{max}) at the maximum indentation depth (h_{max}) to a zero load. The hardness is proportional to the maximum load divided by the square of the contact depth. The hardness and reduced elastic modulus variation with indentation depth (h) are measured using a series of cyclic load-unloading curves to assess the effects of substrate-material hardness, work hardening in the coating during deformation, etc. The 0.1-to-5 mN

load-unloading cycles are obtained at nine different positions on each sample surface using a Bruker-Nano-CETR universal nanomaterial tester (UNMT) that is equipped with a Nanoindentation (NI) module. Unloading to 10% of the initial load is conducted at each load increment up to the final 5 mN load wherein complete unloading to a zero load occurs.

A second mechanical test method is the tapping mode (Useinov, 2004; Gogolinski et al., 2004) of an atomic force microscope. This method is used to provide an independent confirmation of the nanoindentation elastic modulus measurements for several samples. In the tapping mode test, the reduced elastic modulus (E^*) is measured during elastic loading as opposed to the unloading portion of the nanoindentation load-displacement curve after plastic deformation has occurred. The surface displacement of the coating in the tapping mode is caused by contact with the cantilever-mounted diamond tip probe. Loading is applied as an oscillating motion of the probe tip is brought in contact with the surface. The elastic regime is found as the amplitude (A_m) of motion is reduced to less than 1 nm from the initial amplitude set at 5 nm. In general, elastic deformation is measured for a variety of materials at surface displacements of only 2-20 nm. A linear variation between the square of the change in resonant frequency shift (Δf_r)² of the cantilever-tip probe with vertical displacement (z) is equal to the parameter α^2 . It is well demonstrated (Useinov, 2004; Gogolinski et al., 2004) that α is directly proportional to E^* through a power-law relationship, i.e. α equals $(E^*)^n$ where $n \approx 1/2$. Therefore, the elastic modulus E of an unknown material can be determined from a calibration curve that is established from measurements using the known elastic moduli of materials such as polycarbonate at 3.5 GPa, fused silica at 71.7 GPa, Si(100) at 130 GPa, Si(111) at 188 GPa, Ni(111) at 305 GPa, and W(110) at 410 GPa. The tapping-mode calibration curve and elastic modulus measurements of the $\text{Cu}_{1-x}\text{Ni}_x\text{-C}$ nanocomposite coatings are accomplished using the UNMT equipped with a Nanoanalyzer (NA) module. In this study, the contact probe used is a Berkovich diamond tip.

3. Results and Analysis

3.1 Structure and Morphology

The use of HREM provides a detailed look at the different morphologies of the $\text{Cu}_{1-x}\text{Ni}_x\text{-C}$ nanocomposite structures. The transition in growth morphology between distinct layering, the dispersion of nanoparticles, and interpenetrating matrices is seen in the HREM cross-section images of Figures 1a-e where the metal-rich regions are dark and the carbon regions are light in appearance. The immiscibility of C in pure Cu leads to the formation of 3–6 nm grain size, crystalline Cu and amorphous C regions in Figure 1a. The limited solubility (< 3%) of C within Ni leads to the apparent formation of 3 nm-size $\text{Cu}_{0.66}\text{Ni}_{0.34}$ regions that appear to be better interconnected within a matrix of amorphous C in Figure 1c, where similar morphologies appear in Figures 1b-d. The formation of well-defined layered growth morphology appears in the Figure 1e image of the Ni/C nanolaminate coating.

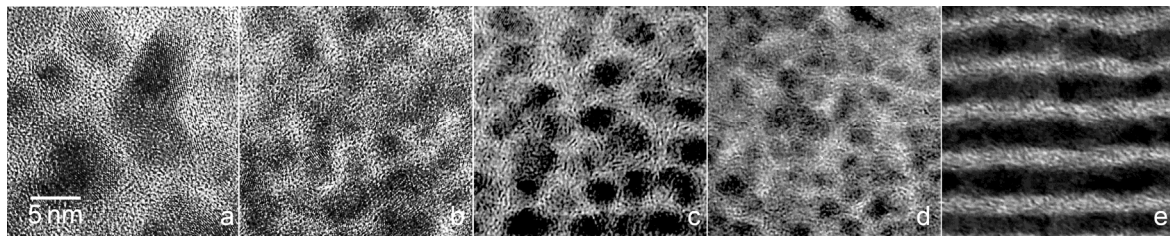


Figure 1. The $\text{Cu}_{1-x}\text{Ni}_x\text{-C}$ nanocomposite coatings are shown as imaged in cross-section using high resolution, transmission electron microscopy where the Ni content (x) equals (a) 0, (b) 0.12, (c) 0.34, (d) 0.45, and (e) 1

The XRD $\theta/2\theta$ scans provide evidence for the presence of crystalline Cu and Ni regions as well as the periodic layered nanostructure when present. The broad Bragg reflections from the Figure 2 high-angle $\theta/2\theta$ scans indicate the metals within the $\text{Cu}_{1-x}\text{Ni}_x\text{-C}$ nanocomposites are nanocrystalline as seen in the HREM images of Figure 1. The carbon component to all of the Cu(Ni)-C composites is most likely to be amorphous, i.e. a diamond-like form of carbon (dlc), as is typically found (Robertson, 2002) for most sputtered carbon films. Evidence of a 2θ peak near 26.0° in Figure 2 could be representative of a (00.2) reflection that can often be found for the graphitic turbostratic form of carbon or an escape peak from the adjacent doped-Si(111) Bragg reflection at 28.4° . The Cu and Ni components have a primary (111) texturing that is common for dense-packed columnar growth of face-centered-cubic (fcc) metals in the Ni-C and Cu(Ni)-C nanocomposite structures. However, the addition of a (110) reflection is found for the high Cu-content deposits as, e.g., in the Cu-C

nanocomposite that is consistent with the polycrystalline particulate structure as shown in Figure 1a.

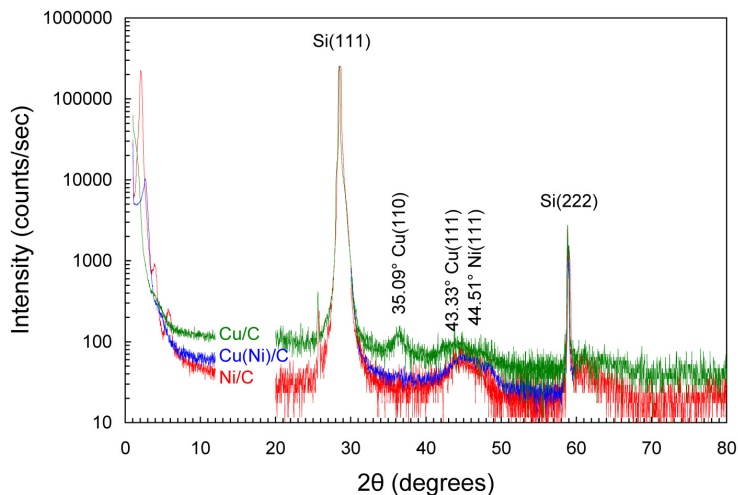


Figure 2. The x-ray diffraction scans are shown of the Cu-C, Cu(Ni)-C and Ni-C nanocomposite coatings

The glancing angle reflections representative of short-range order at $2\theta < 12^\circ$ are presented in the high resolution XRD scans of Figures 3-5. The experimental results are obtained using unpolarized incident radiation, and the simulated reflectivity patterns are modeled assuming a layered structure exists. The simulations are plotted on a reflected intensity scale that is quantitatively calibrated to the measured intensity of the incident x-ray beam in each experiment, i.e. where the direct beam has 100% intensity. The simulation uses λ , σ , and Γ values that are best fit the measured intensity and peak position of the first-order ($n=1$) and higher-order ($n>2$) reflections. The positions of the experimental reflections are indicated on each scan in Figures 3-5 with a vertical dashed line.

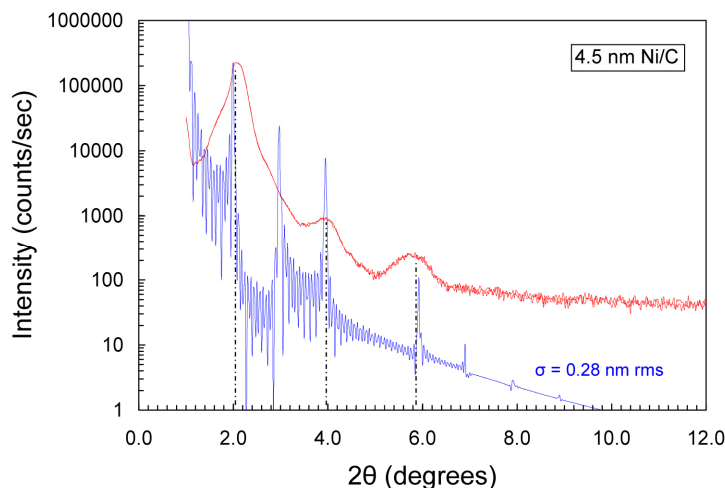


Figure 3. The glancing angle x-ray diffraction scan of the Ni-C nanocomposite sample is shown with a simulation that includes the layer pair spacing and interface roughness

In Figure 3, the design of a 24 layer pair (N), 4.5 nm repeat spacing Ni/C nanolaminate coincides with a best-fit simulation that uses a 4.49 nm layer spacing ($\lambda_{\text{Ni-C}}$), a $l_{\text{Ni}}:\lambda_{\text{Ni-C}}$ ratio (Γ_{Ni}) of 0.40, and a *rms*-interface roughness ($\sigma_{\text{Ni-C}}$) of 0.28 nm. These simulation results indicate a well-defined nanolaminate structure with a 1-2 monolayer thick interface that is seen to be well defined in the HREM image of Figure 1e. In Figure 4, the experimental design of a 75 layer pair (N) Cu/C nanolaminate with a nominal 3.0 nm layer spacing ($\lambda_{\text{Cu-C}}$), and a $l_{\text{Cu}}:\lambda_{\text{Cu-C}}$ ratio (Γ_{Cu}) of 0.35 is best fit with a *rms*-interface roughness ($\sigma_{\text{Cu-C}}$) of 1.26 nm. From the HREM image of Figure 1a, it

is clear that the layering is neither continuous nor well defined. The Cu/C simulation is used for illustrative purposes only, in order to obtain some quantification of an effective roughness, i.e., the extensive interface mixing that has disrupted layer formation and produced a growth structure with particulate dispersion. A curve fit for a 0.4 nm *rms* roughness is shown in Figure 4 to illustrate what would have resulted for a layered structure – the appearance of well-defined first ($n=1$), second ($n=2$), and third ($n=3$) order reflections as opposed to the weak reflections that are observed in the experimental curve. The fitted $\sigma_{\text{Cu-C}}$ parameter value of 1.26 nm indicates an interface thickness that would have equaled the design (but absent) Cu layer thickness itself.

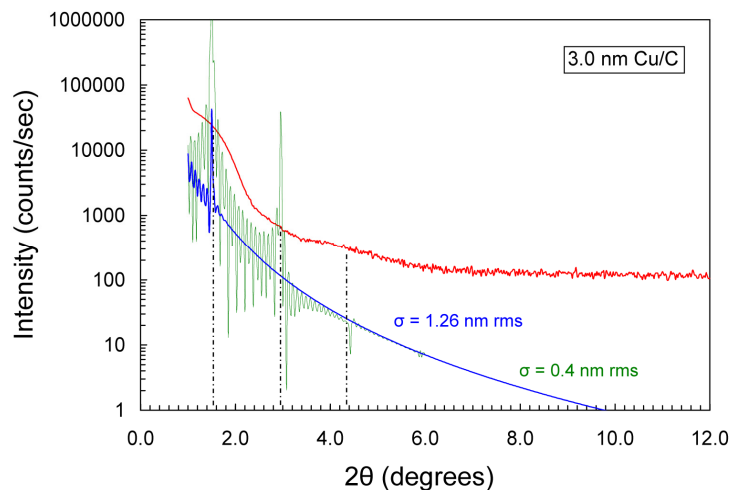


Figure 4. The glancing angle x-ray diffraction scan of the Cu-C nanocomposite coating is shown along with a simulation that includes the nominal layer spacing and an effective interface roughness

In Figure 5, the experimental design of a nominal 30 layer pair (N) Cu(Ni)/C nanolaminate with a 3.4 nm layer spacing ($\lambda_{\text{Cu(Ni)-C}}$), and a $(\ell_{\text{Cu}} + \ell_{\text{Ni}}) : \lambda_{\text{Cu(Ni)-C}}$ ratio $\Gamma_{\text{Cu(Ni)}}$ of 0.35 is best fit with an apparent 3.34 nm periodicity and a *rms*-interface roughness ($\sigma_{\text{Cu(Ni)-C}}$) of 0.53 nm. The $\sigma_{\text{Cu(Ni)-C}}$ value is almost equal to one-half the thickness of the Cu(Ni) layer itself. This large σ -value indicates the layering is not well defined, and in this case the simulation can't be used solely to describe the morphology. The HREM image of Figure 1c shows some indication of periodicity, in the growth direction, to a distribution of Cu(Ni) particles along layer-like bands.

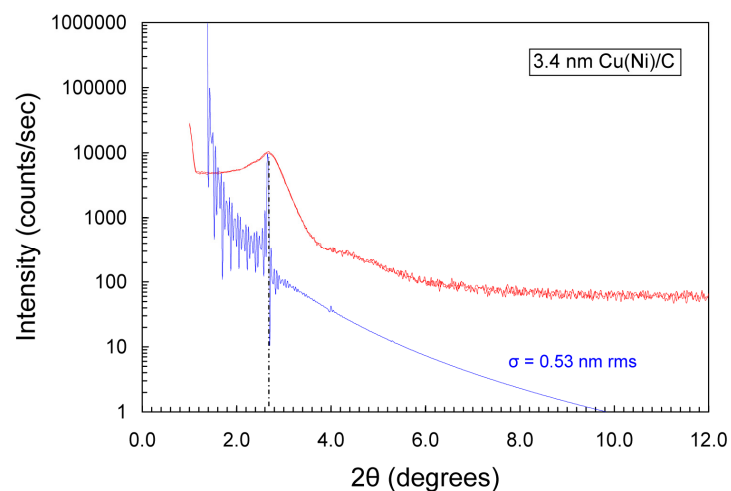


Figure 5. The glancing angle x-ray diffraction scan of the Cu(Ni)-C nanocomposite coating is shown along with a simulation that includes the nominal layer spacing, and modeling of an effective interface roughness

All of the nominal layer thickness (ℓ) values and the dimensional parameters of λ , Γ , and σ that are best fit to the

XRD measurements of the nanocomposite samples are summarized in Table 1. The sample listing is organized with respect to increasing Ni content (x) within the nominal Cu(Ni) layer.

Table 1. The dimensional parameters of layer pair spacing λ , nominal Ni and Cu thickness ℓ , the metal layer to layer pair ratio Γ , and the interface roughness σ for the $\text{Cu}_{1-x}\text{Ni}_x\text{-C}$ nanocomposite coatings

	λ (nm)	ℓ_{Cu} (nm)	ℓ_{Ni} (nm)	x	$\Gamma_{\text{Cu(Ni)}}$	σ (nm)
Cu-C	3.0	1.0	0	0	0.33	1.26
Cu(Ni)-C-2	2.2	0.7	0.1	0.12	0.35	0.81
Cu(Ni)-C	3.4	0.8	0.4	0.34	0.35	0.53
Cu(Ni)-C-3	2.5	0.5	0.4	0.45	0.38	0.73
Ni-C-2	3.4	0	1.2	1	0.36	0.44
Ni-C	4.5	0	1.8	1	0.40	0.28

3.2 Mechanical Properties

The cyclic load-displacement curves obtained by nanoindentation are plotted in Figure 6 as representative for several of the $\text{Cu}_{1-x}\text{Ni}_x\text{-C}$ nanocomposite coatings. A typical nanoindentation cycle with nine load increments is shown for each sample as these measurements are repeated at nine different locations on the coating surface. The cyclic load-displacement curves in Figure 6 are offset on the indentation depth (h) axis to ease the viewing and to separate the results for each sample. The h_{max} values at 5 mN for the Cu-C, Cu(Ni)-C, and Ni-C nanocomposite coatings are 0.219, 0.148, and 0.154 μm , respectively. Evidence of work hardening is found at higher loads where a slight hysteresis occurs in the sequential load cycle as, e.g., for the Cu/C sample in the loading cycles to P_{max} loads of 2 and 3 mN. The H and E^* values for each of the Figure 6 load-unloading curves are plotted as a function of h in Figures 7-8 for the Cu-C, Cu(Ni)-C, and Ni-C nanocomposite coatings. The computation of the E -values for each nanocomposite from the measured E^* -values is made using the standard $(1-\nu_i^2)/E_i$ value of 0.0008 GPa^{-1} for the diamond indenter (i), and a Poisson ratio (ν) of 0.25 for all of the $\text{Cu}_{1-x}\text{Ni}_x\text{-C}$ coatings.

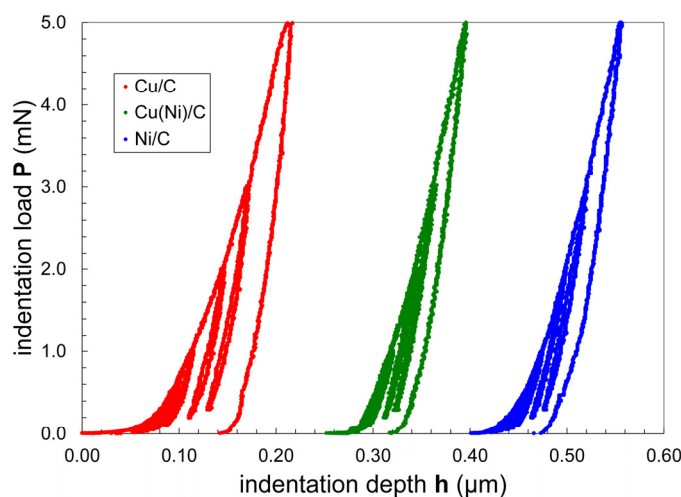


Figure 6. The cyclic load (P) versus nanoindentation depth (h) curves are shown (left-to-right) for the Cu-C, Cu(Ni)-C, and Ni-C nanocomposite coatings

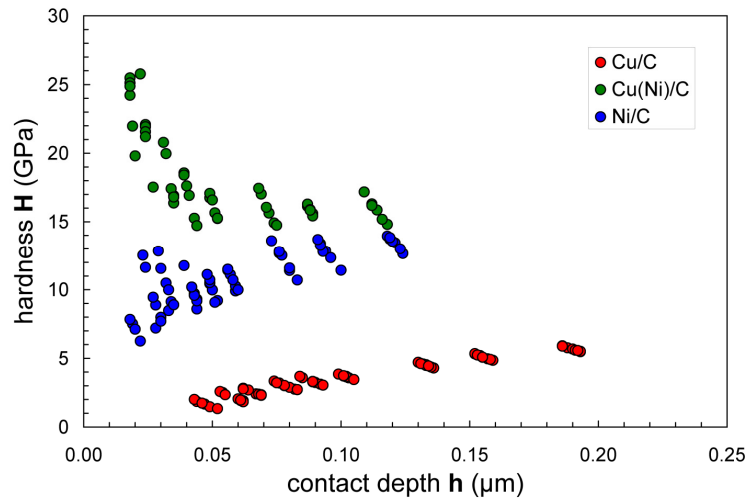


Figure 7. The results for hardness (H) plotted as a function of contact depth (h_c) are shown (top-to-bottom) for the Cu(Ni)-C, Ni-C, and Cu-C nanocomposite coatings

In Figure 7, it is seen that the Cu(Ni)-C nanocomposite has an average surface hardness of 24 ± 2 GPa at contact depths less than 25 nm. In comparison, the Ni-C and Cu-C nanocomposites have surface hardness values of only 7-12 GPa and 1.7 ± 0.4 GPa, respectively. The variation in the Ni-C results appears to be dependent upon the specific regions of the surface that are probed wherein each of the nine indents is separated by 50-100 μm . The H -values for Ni-C are found to range from a lower bound that is typical for nanocrystalline (nc) Ni at 6-8 GPa (Jankowski, 2008) to upper bound values that are an average for a mixture of nc Ni and dlc C (Robertson, 2002). The measured H -values of 2-4 GPa for Cu-C are typical as reported (Jankowski, 2008) for nc Cu. It is seen in Figure 7 that as the indentation depth increases, the H -values begin to converge towards the known hardness for Silicon at ~ 10 GPa. A similar plot is shown in Figure 8 for the E^* -values variation with indentation depth. Here, the Cu(Ni)-C coating has a greater reduced modulus of 138 ± 9 GPa in comparison with the Ni-C and Cu-C coatings that have E^* -values of 84 ± 3 GPa and 43 ± 4 GPa, respectively. It is seen in Figure 8 that as the indentation depth increases, the E^* -values converge towards the established E^* -value of Si(111) at ~ 175 GPa.

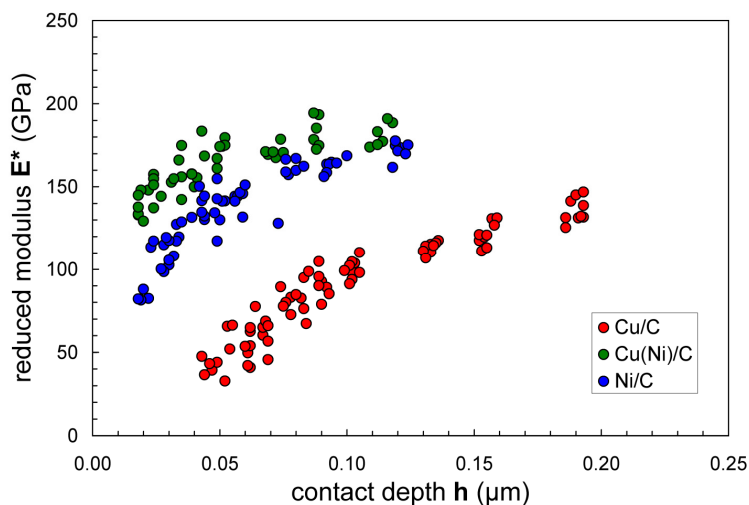


Figure 8. The results for reduced modulus (E^*) plotted as a function of contact depth (h_c) are shown (top-to-bottom) for the Cu(Ni)-C, Ni-C, and Cu-C nanocomposite coatings

The tapping-mode measurement of the known material standards provides a calibration-curve relationship for E^* (GPa) as a function of α . The calibration equation derived for this particular Berkovich-tip cantilever probe is

$$E^* = (0.227 \cdot \alpha)^{1.87} \quad (1)$$

The values measured for α (Hz-nm^{-1/2}) are listed in Table 2 for several of the Cu_{1-x}Ni_x-C coatings along with the corresponding E^* -values that are computed using Equation (1). The measured α -values for fused silica and Si(100) are listed in Table 2 as well since these samples form part of the calibration material set that is used to fit the coefficient and power law exponent of the Equation (1), and because fused silica and Si(100) have elastic moduli similar to the nanocomposite coatings under investigation. It's important to note that the α -values for fused silica and Si(100) do not necessarily rest on the curve fit of Equation (1) since these materials help define the calibration curve along with the other reference materials. The E -values for the tapping-mode Nanoanalyzer (NA) results are then computed using the $(1-\nu_i^2)/E_i$ standard value of 0.0008 GPa⁻¹ for the diamond indenter (i) as was determined for the nanoindentation (NI) tests.

Table 2. The reduced modulus E^* , elastic moduli E , and hardness H of the Cu_{1-x}Ni_x-C nanocomposite coatings

	H (GPa)	E_{NI}^* (GPa)	E_{NI} (GPa)	H^3/E_{NI}^2 (GPa)	α (Hz-nm ^{-1/2})	E_{NA}^* (GPa)	E_{NA} (GPa)
Cu-C	1.7 ± 0.4	43 ± 4	42	0.003	39.2 ± 1.2	59.5 ± 3.5	58
Cu(Ni)-C-2	27 ± 1	159 ± 5	169	0.69	-	-	-
Cu(Ni)-C	24 ± 2	138 ± 5	144	0.67	61.5 ± 2.1	138.3 ± 8.9	145
Cu(Ni)-C-3	11 ± 1	150 ± 8	158	0.05	-	-	-
Ni-C-2	25 ± 5	194 ± 3	214	0.34	-	-	-
Ni-C	7-12	84 ± 3	84	0.05-0.24	47.2 ± 1.6	84.5 ± 5.4	85
fused silica	9.0 ± 0.2	69 ± 1	71	0.14	40.0 ± 0.7	70.1 ± 2.3	72
Si(100)	9.9 ± 0.2	130 ± 2	132	0.06	55.9 ± 1.0	127.4 ± 4.3	130

The tapping-mode NA-measurements of elastic modulus closely match the nanoindentation NI-values at indentation depths less than 25 nm confirming the NI-hardness values. It can be deduced that there are no significant indentation size effects (ISE) present for the measurements of E (and H as well) within the indentation depths that are approximately equal to or less than ~10% of the coating thickness. ISE(s) are attributed typically to the presence of singular grain boundaries and/or densities of defects such as dislocations within the indentation that are not representative of the structure at large which can produce E and H values that appear too high or too low versus the actual values.

4. Discussion

The transition in growth morphology from a dispersion of Cu nanoparticles within a C matrix, through a Cu(Ni)-C interpenetrating-type matrix structure, to a Ni-C layered structure is controlled by the Cu(Ni) alloy content. In this specific sequence of morphological transition, the Ni content is increased during the Cu deposition. Ni is the addition that is soluble with both of the base materials, i.e. Cu and C. The complete solubility of Ni in Cu, and the partial solubility of C in Ni lead to this progression in structural morphology in the otherwise completely immiscible Cu-C system. Similar effects are reported (Eisenmenger-Sittner et al., 1995) elsewhere for the Al-Pb system. A distribution of Pb-based particles forms within a continuous matrix during the laminate deposition of these two immiscible metal components. It is suggested that the minimization of the chemical potential leads to islanding from phase separation during the growth process.

The reduced elastic modulus (E^*) and Young's modulus (E) of the Cu_{1-x}Ni_x-C nanocomposite coatings are determined from both the nanoindentation (NI) and the Nanoanalyzer (NA) tapping mode tests. The E_{NI} and E_{NA} moduli measurements are consistent with those values (Trent et al., 1972; Yamada-Takamura et al., 1999; Frederikse, 2008) that correspond with polycrystalline forms of the Cu, Ni, and C components. For example, since Ni and Cu are both anisotropic, the lowest E -values are found along the [100] at 129 GPa and 66 GPa, respectively. In comparison, the values along [111] for Ni and Cu are 304 GPa and 192 GPa, respectively. For polycrystalline Cu-Ni, a value of 162 GPa can be expected that is close to the elastic modulus measured for the three Cu(Ni)-C nanocomposite coatings. The diamond-like/amorphous form of carbon can have an elastic modulus that may range from 70-400 GPa or more (Schneider et al., 1993; Brand et al., 2002; Robertson, 2002) as dependent upon synthesis conditions, its mass density, and impurity content. Modulus values of 200-300 GPa

are typical for dlc sputter deposits with densities of 2.1-2.3 gm·cm⁻³. Thus, the elastic response of the Cu-C and Ni-C nanocomposite coatings trend towards the values found for the metallic components. These results indicate that the initial elastic response is dominated by the metal component which tends to behave as though it is continuous throughout the structure. A polycrystalline nature to the Cu structure is indicated in the XRD scans of Figure 2 by the presence of (111) and (110) reflections. The appearance of a broad (111) peak for Ni is consistent with the columnar growth structure for a layered growth. Porous, i.e. not fully dense, forms of metals will have elastic moduli that are less (Gibson, 2000) than the values for fully dense metals discussed previously.

The hardness values of the Cu-C and Ni-C nanocomposite samples appear to be largely representative of the constituent nanocrystalline metal components. A higher hardness and modulus value is measured for the Ni-C-2 sample than for the Ni-C sample as perhaps due to a refined grain size along with a greater disruption of the layer growth as evidenced in the increased interface roughness σ -values in Table 1. The higher hardness values are again seen in for the Cu(Ni)-C and Cu(Ni)-C-2 nanocomposite samples but with a decreased value of modulus in comparison with Ni-C-2. The slightly greater modulus and hardness measured for Cu(Ni)-C-2 sample in comparison to the Cu(Ni)-C nanocomposite may be attributed to the smaller grain size within the metal matrix component and its disrupted layer growth as seen in Figures 1b-c. The higher hardness values for these three samples provide indication of composition and morphological effects on the deformation behavior. In the HREM image of Figure 1a, the Cu component appears to have agglomerated into larger nanoparticles within regions of the Cu-C nanocomposite, thereby dominating the hardness as well as the initial elastic response described above. In comparison, the C component appears to have better continuity throughout the Cu(Ni)-C coating in Figure 1c, thereby providing a significant contribution to the high hardness behavior of this nanocomposite. In combination with the elastic response indicative of a metallic dominated response, it can be postulated that the Cu(Ni)-C structure is likely to be uniquely composed of interpenetrating matrices of Cu(Ni) and C. The lower Ni content nanocomposites of Cu(Ni)-C and Cu(Ni)-C-2 both evidence high hardness with a modulus that is lower in comparison the Ni-C-2 nanocomposite. For the larger nominal layer pair spacing found in the Ni-C nanocomposite, a clear nanolaminate is formed as seen in Figure 1e where the elastic and plastic behavior is then initially dominated by the more compliant Ni. The 144 GPa elastic modulus of the Cu(Ni)-C nanocomposite and 169 GPa modulus of the Cu(Ni)-C-2 sample show values that are similar to a polycrystalline Cu-Ni alloy as mentioned above. These results again suggest that the metal component is primarily responsive in the elastic loading in these nanocomposites.

The measurement of a H/E ratio of 1/6 differs significantly from the ratio of 1/10 or less as found for hard (> 20 GPa) and superhard (>40 GPa) coatings. The H/E ratio is significant with respect to the assessment (Musil, 2000) of wear resistance for hard nanocomposite coatings. Typical H/E values for diamond cutting tool surfaces (Hu et al., 2007) as well as many nanomaterials with high melting points such as borides, carbides, and nitrides are reported (Leyland & Matthews, 2000; Andrievskiy, 2007) to range from 1/9 to 1/15 or less. Single-phase coatings, nanolaminates, and particle-reinforced composites are common for high hardness coatings wherein values greater than 20-25 GPa are often accompanied by higher stiffness values. The H^3/E^2 value is correlated (Musil, 2000) with the material resistance to plastic deformation, hence wear. Using the Table 2 data, the H^3/E^2 values computed for the Cu(Ni)-C and Cu(Ni)-C-2 nanocomposite coatings at 0.67-0.69 GPa are twice as high as for any other nanocomposite coating (Musil, 2000) with a surface hardness below 30 GPa. Although not as high as for the Cu(Ni)-C coating, the H^3/E^2 value for the Ni-C and Ni-C-2 samples trend towards the greatest H^3/E^2 value reported previously (Musil, 2000) for any other nanocomposite coating with a hardness below 25 GPa. Along with the electron microscopy and x-ray diffraction results, the Cu(Ni)-C coating provides an example of a new type of two-phase nanocomposites with the structural feature of interpenetrating-matrix components that can provide high hardness without high stiffness.

5. Conclusions

The Cu_{1-x}Ni_x-C nanocomposites with a Cu(Ni) metal layer to nominal Cu(Ni)/C layer pair thickness ratio (I) of 0.35-0.4 show a morphological transition that departs from a well-defined nanolaminate growth as the Ni content (x) ratio is progressively reduced. A morphology effect on the nanoindentation hardness (H) and Young's modulus (E) is measurable for these nanocomposite coatings. An increase in the H^3/E^2 value is measured for interpenetrating distributions of Cu(Ni) and C within an x composition range of 0.12-0.33 as, e.g., a 24 GPa hardness and 144 GPa elastic modulus. A transition in morphology at the nanoscale has lead to a high hardness, yet compliant Cu(Ni)-C nanocomposite with a high H/E ratio of 1/6 and a high H^3/E^2 value of 0.67 GPa.

Acknowledgments

This work was supported in part by the J. W. Wright Endowment for Mechanical Engineering and a Terry and Linda Fuller Foundation Grant at Texas Tech University.

References

- Andrievskiy, R. A. (2007). New Superhard Nanomaterials-Based High-Melting Point Compounds. *Proc. 17th Int. Offshore Polar Eng. Conf.*, 4, 2875-2880.
- Brand, J., Beckmann, Blug, B., Konrath, G., & Hollstein, T. (2002). Diamond-like carbon coatings—a new design element for tribological applications. *Indus. Lubr. Tribol.*, 54, 291-295. <http://dx.doi.org/10.1108/00368790210697868>
- Chang, S. Y., Lin, S. Y., Huang, Y. C., & Wu, C. L. (2010). Mechanical properties, deformation behaviors and interface adhesion of (AlCrTaTiZr)_{N_x} multi-component coatings. *Surf. Coat. Technol.*, 204, 3307-3314. <http://dx.doi.org/10.1016/j.surfcoat.2010.03.041>
- Eisenmenger-Sittner, C., Behr, R., Bergauer, A., Hejl, A., & Bauer, W. (1995). A Multilayer Approach to the Design of Fine Dispersed Metallic Two Component Materials. in *Structure and Properties of Multilayered Thin Films*. In T. D. Nguyen, B. M. Lairson, B. M. Clemens, S. C. Shin, & K. Sato (Eds.), *Mater. Res. Soc. Symp. Proc.*, 382, 141-146.
- Fischer-Cripps, A. C., Bull, S. J., & Schwarzer, N. (2012). Critical review of claims for ultra-hardness in nanocomposite coatings. *Phil. Mag.*, 92, 101-1630. <http://dx.doi.org/10.1080/14786435.2011.652688>
- Frederikse, H. P. R. (2008). Elastic Constants of Single Crystals. in *CRC Handbook 88th edn.* (Sec. 12, pp. 33-38). D. R. Lide (ed.), Boca Raton: CRC Press.
- Gibson, L. J. (2000). Mechanical behavior of metallic foams. *Ann. Rev. Mater. Sci.*, 30, 191-227.
- Gogolinski, K. V., Kosakovskaya, Z. Y., Useinov, A. S., & Chaban, I. A. (2004). Measurement of the Elastic Moduli of Dense Layers of Oriented Carbon Nanotubes by a Scanning Force Microscope. *Acoust. Phys.*, 50, 664-669. <http://dx.doi.org/10.1134/1.1825096>
- Hu, J., Chou, Y. K., Thompson, R. G., Burgess, J., & Street, S. (2007). Characterizations of nanocrystalline diamond coating cutting tools. *Surf. Coat. Technol.*, 202, 1113-1117. <http://dx.doi.org/10.1016/j.surfcoat.2007.07.050>
- Jankowski, A. F., & Stearns, D. G. (1991). Layer Formation in CuNi/C X-Ray Optics. In *Evolution of Thin Film and Surface Microstructure*. C. Thompson, J. Tsao, & D. Srolovitz (Eds.), *Mater. Res. Soc. Symp. Proc.*, 202, 695-700.
- Jankowski, A. F., Wall, M. A., Hayes, J. P., & Alexander, K. B. (1997). Properties of Boron/Boron-Nitride Multilayers. *NanoStructured Materials*, 9, 467-471. [http://dx.doi.org/10.1016/S0965-9773\(97\)00102-5](http://dx.doi.org/10.1016/S0965-9773(97)00102-5)
- Jankowski, A. F. (1999). Nanohardness and chemical bonding of boron nitride films. *Thin Solid Films*, 343-344, 238-241. [http://dx.doi.org/10.1016/S0040-6090\(98\)01634-4](http://dx.doi.org/10.1016/S0040-6090(98)01634-4)
- Jankowski, A. F. (2008). Vapor Deposition and Characterization of Nanocrystalline Nanolaminates. *Surf. Coatings Technol.*, 203, 484-489. <http://dx.doi.org/10.1016/j.surfcoat.2008.06.110>
- Kohn, V. G. (1995). On the theory of reflectivity by an x-ray multilayer mirror. *Phys. Stat. Sol. (B)*, 187, 61-70. <http://dx.doi.org/10.1002/pssb.2221870105>
- Leyland, A., & Matthews, A. (2000). On the significance of the *H/E* ratio in wear control: a nanocomposite coating approach to optimized tribological behavior. *Wear*, 246, 1-11. [http://dx.doi.org/10.1016/S0043-1648\(00\)00488-9](http://dx.doi.org/10.1016/S0043-1648(00)00488-9)
- Musil, J. (2000). Hard and superhard nanocomposite coatings. *Surf. Coat. Technol.*, 125, 322-330. [http://dx.doi.org/10.1016/S0257-8972\(99\)00586-1](http://dx.doi.org/10.1016/S0257-8972(99)00586-1)
- Oliver, W. C., Pharr, G. M. (1992). An improved technique for determining hardness and elastic modulus using load and displacement sensing indentation experiments. *J. Material Research*, 7, 1564-1583. <http://dx.doi.org/10.1557/jmr.1992.1564>
- Oliver, W. C., Pharr, G. M. (2004). Measurement of hardness and elastic modulus by instrumented indentation: Advances in understanding and refinements to methodology. *J. Material Research*, 19, 3-20. <http://dx.doi.org/10.1557/jmr.2004.19.1.3>

- Robertson, J. (2002). Diamond-like amorphous carbon. *Mater. Sci. Eng. R*, 37, 129-281. [http://dx.doi.org/10.1016/S0927796X\(02\)00005-0](http://dx.doi.org/10.1016/S0927796X(02)00005-0)
- Schneider, D., Scheibe, H. J., Schwarz, Th., & Hess, P. (1993). Characterization of thin diamond-like carbon films by ultrasonic waves. *Diamond Rel. Mater.*, 2, 1396-1401. [http://dx.doi.org/10.1016/0925-9635\(93\)90147-T](http://dx.doi.org/10.1016/0925-9635(93)90147-T)
- Trent, H. M., Stone, D. E., & Beaubien, L. A. (1972). Elastic Constants, Hardness, Strength, Elastic Limits, and Diffusion Coefficients of Solids. *American Institute of Physics Handbook* (Sec. 2e, pp. 49-59). R. K. Cook (ed.), New York, NY: McGraw Hill.
- Useinov, A. S. (2004). A Nanoindentation Method for Measuring the Young Modulus of Superhard Materials Using a NanoScan Scanning Probe Microscope. *Instrum. Exp. Tech.*, 47, 119-123. <http://dx.doi.org/10.1023/B:INET.0000017264.83566.69>
- Veprek, S., & Veprek-Heijman, M. G. J. (2012). Limits to the preparation of superhard nanocomposites: Impurities, deposition and annealing temperature. *Thin Solid Films*, 522, 274-282. <http://dx.doi.org/10.1016/j.tsf.2012.08.048>
- Yamada-Takamura, Y., Shimono, E., & Toshida, T. (1999). Nanoindentation characterization of cBN films deposited from vapor phase. In M. Hrabovsky, et al. (Eds.), *Symp. Proc. 14th International Symp. Plasma Chemistry ISPC-14* (Vol. 3, pp. 1629-1634). Prague: Tschechien.
- Zhang, S., & Zhang, X. (2012). Toughness evaluation of hard coatings and thin films. *Thin Solid Films*, 520, 2375-2389. <http://dx.doi.org/10.1016/j.tsf.2011.09.036>